Phase detection limits in off-axis electron holography from pixelated detectors: gain variations, geometric distortion and failure of reference-hologram correction

Martin Hÿtch, Christophe Gatel

Phase detection limits in off-axis electron holography from pixelated detectors: gain variations, geometric distortion and failure of reference-hologram correction

M. J. Hÿtch and C. Gatel

CEMES, Université de Toulouse, CNRS, 29 rue Jeanne Marvig, 31055 Toulouse, France

Abstract

We investigate the effect that recording off-axis electron holograms on pixelated detectors, such as charge-coupled devices (CCD) and direct-detection devices (DDD), can have on measured amplitudes and phases. Theory will be developed for the case of perfectly uniform interference fringes illuminating an imperfect detector with gain variations and pixel displacements. We will show that both these types of defect produce a systematic noise in the phase images that depends on the position of the holographic fringes with respect to the detector. Subtracting a reference hologram from the object hologram will therefore not remove the phase noise if the initial phases of the two holograms do not coincide exactly. Another finding is that pi-shifted holograms are much less affected by gain variations but show no improvement concerning geometric distortions. The resulting phase errors will be estimated and simulations presented that confirm the theoretical developments.

Introduction

In electron holography, there is a continual quest to improve the precision and accuracy of phase measurements [1-7]. This is particularly the case at medium resolution where the phase is directly related to the local field strengths measured in quantitative experiments, whether they be electric [8, 9, 10], magnetic [11, 12] or crystalline strain [13, 14]. Most attention has been focussed on the detection limits imposed by the random errors caused by counting statistics [15]. However, there are also many other sources of error, more often systematic in nature, such as specimen interactions and preparation artefacts, optical parameters, hologram processing and the main object of this paper, the detector characteristics. With the advent of almost unlimited exposure times [16], systematic errors will determine the ultimate accuracy, and even precision in some sense, of electron holography experiments.

Random errors indeed arise essentially from the counting statistics. Electron holograms are acquired with a finite number of electrons which leads inevitably to random fluctuations in the

measured intensities, which in turn leads to noise in the reconstructed phase images [15]. Numerous papers, both theoretical and experimental, have been dedicated to the phase detection limits imposed by counting statistics. They show that the noise is random and can be reduced by increasing the electron dose [3, 4, 7].

Systematic errors come from various sources, first and foremost being the sample under investigation. Whilst the sample is providing the fields we are trying to measure, real specimens also introduce a number of additional phenomena which can produce systematic shifts in the phase. An uneven sample thickness can introduce unwanted phase variations through the action of the mean-inner potential of the material [8] or dynamic diffraction effects [17]. Sample charging under the electron beam also produces spurious phase variations [18, 19, 20] and damage from specimen preparation may diminish the phase change from electric fields in a systematic way [9, 21, 22].

A number of artefacts arise from the imaging conditions, such as the curvature of the elliptic incident wave [23] or from charging of biprisms or their associated Fresnel fringes when used singly [24]. The projector lenses of the microscope will introduce long-range phase changes, just like in high-resolution electron microscopy [25]. Finally, the detector introduces systematic phase variations from the packing of the fibre-optic coupling of charge-coupled devices (CCD) [1, 6].

The best way to deal with systematic errors is of course to eliminate them at the source, such as employing better sample preparation techniques [22] or using two biprisms to avoid almost entirely Fresnel fringes in holograms [26]. To correct for the remaining systematic errors, the standard procedure is to acquire a reference hologram taken in a field-free region of the vacuum [1]. Apart from sample artefacts (and Fresnel fringes) the method is considered robust for all other systematic errors. In this paper, we will show that for pixelated detectors, such as CCDs or direct-detection devices (DDD), a single reference hologram is not sufficient and will furthermore introduce additional systematic errors.

This paper was written in the context of dynamic automation and the stabilisation of holographic fringes [16]. We have shown that controlling the microscope with feedback loops allows us to stabilise the phase of the hologram during very long exposure times, without the need of image stacks [7, 27]. The aim is to reduce significantly the random errors from counting statistics and hence reach the ultimate phase detection limits in electron holography experiments. Of course the dose that samples can submit has a limit. But in some cases, the important factor is the dose rate, meaning that a high number of electrons can be accumulated over very long exposure times at low beam intensity. In addition, some fields are measured in the vacuum where there are no such limitations.

As random errors are gradually squeezed out of experiments, all sources of systematic error must be ascertained and removed. Control of the average phase of the hologram also allows more sophisticated phase reconstruction methods such as the fringe-shifting method [28] used in the pi-shift variant in image stacks [29] or through automation [16]. The method is particularly useful for separating the centre-band from the side-band in the reconstruction process. We will be making use of these possibilities in the theoretical development. We will not consider sample artefacts and implicitly treat measurements carried out in the vacuum either containing stray fields or in field-free reference hologram regions. We will also consider a double biprism configuration was successful in removing the Frensel fringes [26]. The only remaining source of error is the detector.

Pixelated digital detectors, originally in the form of CCD and now DDD, have revolutionized electron microscopy [30] and were key to the development of quantitative techniques, in particular electron holography [31]. Nevertheless, they are not perfect and suffer, for example, from non-uniform modulation transfer functions (MTF) or lower than ideal Detective Quantum Efficiency (DQE). Here, we will be examining the consequences for electron holography of two less studied imperfections: gain variations and geometric displacement of pixels.

Theory

The case of a perfectly regular set of interference fringes illuminating a pixelated detector will be studied. In addition, it will be assumed that the signal is sufficiently intense to ignore counting statistics. The input signal, S, can then be described as:

$$S(\boldsymbol{r},\phi) = 1 + 2a\cos(2\pi\boldsymbol{q}.\boldsymbol{r} + \phi) \tag{1}$$

where $\mathbf{q}$ is the carrier frequency vector of the interference fringes, $\mathbf{r}$ the position coordinate on the detector in the *x*-*y* plane, 'a' the amplitude (with this definition equal to half the visibility) of the fringes and ϕ their phase. The amplitude is a real number less than one half and the phase of the fringes will depend on the choice of origin of the coordinate system with respect to the detector. In what follows, the assumed units for $\mathbf{r}$ and $\mathbf{q}$ will be pixels and pixels^{-1} respectively.

For most of the following development, the signal will be expressed in the complex form:

$$S(\boldsymbol{r},\phi) = 1 + ae^{i\phi}e^{2\pi i\boldsymbol{q}.\boldsymbol{r}} + ae^{-i\phi}e^{-2\pi i\boldsymbol{q}.\boldsymbol{r}} \tag{2}$$

which allows easy passage to and from the Fourier-space representation:

$$\tilde{S}(\boldsymbol{k},\phi) = \delta(\boldsymbol{k}) + ae^{i\phi}\delta(\boldsymbol{k}-\boldsymbol{q}) + ae^{-i\phi}\delta(\boldsymbol{k}+\boldsymbol{q}) \tag{3}$$

where $\mathbf{k}$ is the frequency coordinate in Fourier space. The signal is separated into three parts: a centre-band centred at $\mathbf{k} = 0$ and two side bands at $\mathbf{q}$ and $-\mathbf{q}$.

Pi-shifted holograms

We will also be making use of pi-shifted holograms during the development [28]. This consists in recording a second hologram, shifted in phase by exactly pi:

$$\begin{aligned} S(\boldsymbol{r},\phi+\pi) &= 1 + ae^{i\phi+i\pi}e^{2\pi i\boldsymbol{q}.\boldsymbol{r}} + ae^{-i\phi-i\pi}e^{-2\pi i\boldsymbol{q}.\boldsymbol{r}} \\ &= 1 - ae^{i\phi}e^{2\pi i\boldsymbol{q}.\boldsymbol{r}} - ae^{-i\phi}e^{-2\pi i\boldsymbol{q}.\boldsymbol{r}} \end{aligned} \quad (4)$$

If the two hologram signals are summed, we obtain the centre-band only:

$$S^{(+)}(\boldsymbol{r},\phi) \stackrel{\text{def}}{=} S(\boldsymbol{r},\phi) + S(\boldsymbol{r},\phi+\pi) = 2 \quad (5)$$

and subtraction allows the centre-band to be eliminated:

$$S^{(-)}(\boldsymbol{r},\phi) \stackrel{\text{def}}{=} S(\boldsymbol{r},\phi) - S(\boldsymbol{r},\phi+\pi) = 2ae^{i\phi}e^{2\pi i\boldsymbol{q}.\boldsymbol{r}} + 2ae^{-i\phi}e^{-2\pi i\boldsymbol{q}.\boldsymbol{r}} \quad (6)$$

The factor of two indicates that twice as many electrons were used to create the pi-shifted hologram than the single hologram.

Phase reconstruction

The extraction of a side-band from the hologram can be described as follows [32]:

$$\tilde{S}_q(\boldsymbol{k},\phi) \stackrel{\text{def}}{=} \tilde{S}(\boldsymbol{k}+\boldsymbol{q},\phi)\tilde{M}(\boldsymbol{k}) \quad (7)$$

where $\tilde{M}(\boldsymbol{k})$ is the masking function. The mask can take different shapes but will be considered to be real, centrosymmetric and unity at the origin:

$$\tilde{M}(\boldsymbol{k}) = \tilde{M}^*(\boldsymbol{k}), \tilde{M}(\boldsymbol{k}) = \tilde{M}(-\boldsymbol{k}) \text{ and } \tilde{M}(\boldsymbol{0}) = 1 \quad (8)$$

The simplest mask shape is a hard circular mask, with a radius of k_M that we will assume to be less than q/2 in order to separate side-band from centre-band:

$$\forall\, k < k_M, \tilde{M}(\boldsymbol{k}) = 1, \text{otherwise } 0 \quad (9)$$

Another form is the *cosine* mask, which we will be using later to avoid ringing artefacts in the processing of the simulated holograms:

$$\forall\, k < k_M, \tilde{M}(\boldsymbol{k}) = \cos\left(\frac{\pi}{2}\frac{k}{k_M}\right), \text{otherwise } 0 \quad (10)$$

It is easy to show that the two extracted side-bands are conjugate symmetric [32], as for Fourier components of real images:

$$\tilde{S}_{-q}(\boldsymbol{k},\phi) = \tilde{S}_q(\boldsymbol{k},\phi)^* \quad (11)$$

It is therefore only necessary to consider one of the side-bands, the positive one in our case.

Taking the perfect hologram described in Fourier space, Eq. (3), and applying Eq. (7) to extract the side-band and centre-band produces the following trivial result:

$$\tilde{S}_q(\boldsymbol{k},\phi) = \mathrm{a}e^{i\phi}\delta(\boldsymbol{k}) \text{ and } \tilde{S}_0(\boldsymbol{k},\phi) = \delta(\boldsymbol{k}) \quad (12)$$

and in real-space:

$$S_q(\boldsymbol{r},\phi) = \mathrm{a}e^{i\phi} \text{ and } S_0(\boldsymbol{k},\phi) = 1 \tag{13}$$

Naturally, the exact shape of the mask does not matter for perfect fringes with delta-function side and centre-bands.

For the pi-shifted holograms the results for the side-band reconstruction are:

$$S_q^{(-)}(\boldsymbol{r},\phi) = \mathrm{a}e^{i\phi} \text{ and } S_q^{(+)}(\boldsymbol{r},\phi) = 0 \tag{14}$$

and for the centre-band reconstruction:

$$S_0^{(-)}(\boldsymbol{r},\phi) = 0 \text{ and } S_0^{(+)}(\boldsymbol{r},\phi) = 1 \tag{15}$$

This is the expected result from the pi-shifting algorithm: the side-band and centre-band are obtained from the subtracted and summed holograms, respectively. For a uniform and perfect hologram, the process has no interest. However, the technique will be of great value in the presence of spatial variations, allowing the centre and side-bands to be separated.

Gain variations

We will now consider the effect of an imperfect pixelated detector, and firstly with a variable gain. Let the gain, G, be a function of (pixel) position:

$$G(\boldsymbol{r}) = 1 + g(\boldsymbol{r}) \tag{16}$$

where g(**r**) is the deviation from the perfect value of 1 and assumed to have an average of zero. The gain can have both low and high-frequency variations. In this paper, we will be particularly interested in the latter. Later on, the gain will be modelled as random variations, uncorrelated from pixel to pixel, but fixed for a given experiment. The Fourier transform of the gain will therefore be uniformly filled across all frequencies: equivalent to a white noise distribution. The following development will, however, remain general.

For a general signal, S, the image intensity recorded by the detector will be:

$$I(\boldsymbol{r}) = S(\boldsymbol{r})G(\boldsymbol{r}) \tag{17}$$

In Fourier space the gain will be introduced as a convolution:

$$\tilde{I}(\boldsymbol{k}) = \tilde{S}(\boldsymbol{k}) \otimes \tilde{G}(\boldsymbol{k}) \tag{18}$$

which is the source of the complications for the phase reconstruction. For the perfect hologram fringes, the result in Fourier space will be, explicitly:

$$\begin{aligned}\tilde{I}(\boldsymbol{k},\phi) = \tilde{S}(\boldsymbol{k},\phi) \otimes \tilde{G}(\boldsymbol{k}) &= \left(\delta(\boldsymbol{k}) + ae^{i\phi}\delta(\boldsymbol{k}-\boldsymbol{q}) + ae^{-i\phi}\delta(\boldsymbol{k}+\boldsymbol{q})\right) \otimes (\delta(\boldsymbol{k}) + \tilde{g}(\boldsymbol{k})) \\ &= \tilde{S}(\boldsymbol{k},\phi) + \tilde{g}(\boldsymbol{k}) + ae^{i\phi}\tilde{g}(\boldsymbol{k}-\boldsymbol{q}) + ae^{-i\phi}\tilde{g}(\boldsymbol{k}+\boldsymbol{q})\end{aligned} \tag{19}$$

The convolution is illustrated schematically in Figure 1a where the Fourier transform of the gain is convoluted with the centre-band and side-bands to create overlap. After extraction of the positive side-band:

$$\tilde{I}_q(\boldsymbol{k},\phi) = \Big(\delta(\boldsymbol{k}+\boldsymbol{q}) + ae^{i\phi}\delta(\boldsymbol{k}) + ae^{-i\phi}\delta(\boldsymbol{k}+2\boldsymbol{q}) + \tilde{g}(\boldsymbol{k}+\boldsymbol{q}) + ae^{i\phi}\tilde{g}(\boldsymbol{k}) + ae^{-i\phi}\tilde{g}(\boldsymbol{k}+2\boldsymbol{q})\Big)\tilde{M}(\boldsymbol{k})$$

$$= \tilde{M}(-\boldsymbol{q}) + ae^{i\phi}\tilde{M}(\boldsymbol{0}) + ae^{-i\phi}\tilde{M}(-2\boldsymbol{q}) + \tilde{g}(\boldsymbol{k}+\boldsymbol{q})\tilde{M}(\boldsymbol{k}) + ae^{i\phi}\tilde{g}(\boldsymbol{k})\tilde{M}(\boldsymbol{k}) + ae^{-i\phi}\tilde{g}(\boldsymbol{k}+2\boldsymbol{q})\tilde{M}(\boldsymbol{k}) \quad (20)$$

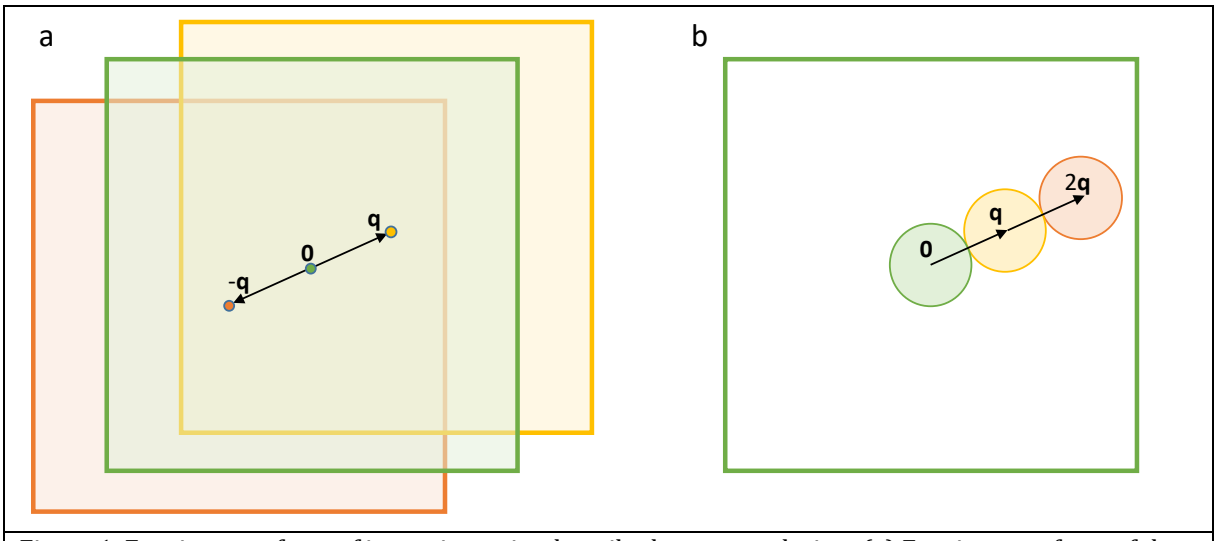

Figure 1. Fourier transform of image intensity described as a convolution: (a) Fourier transform of the gain variation is convoluted with the centre-band (green), positive side-band (yellow) and negative side-band (orange); (b) Contributions to positive side-band from different parts of the Fourier transform of the gain.

Since the mask is zero by design for values of k > q/2, and unity at the origin, some of the terms will disappear:

$$\tilde{I}_q(\boldsymbol{k},\phi) = ae^{i\phi} + \tilde{g}(\boldsymbol{k}+\boldsymbol{q})\tilde{M}(\boldsymbol{k}) + ae^{i\phi}\tilde{g}(\boldsymbol{k})\tilde{M}(\boldsymbol{k}) + ae^{-i\phi}\tilde{g}(\boldsymbol{k}+2\boldsymbol{q})\tilde{M}(\boldsymbol{k}) \quad (21)$$

To simplify the expression, the same definition as for the side-band extraction, Eq. (7), can be exploited to describe the different parts of the gain function:

$$\tilde{I}_q(\boldsymbol{k},\phi) = ae^{i\phi} + \tilde{g}_q(\boldsymbol{k}) + ae^{i\phi}\tilde{g}_0(\boldsymbol{k}) + ae^{-i\phi}\tilde{g}_{2q}(\boldsymbol{k}) \quad (22)$$

The three contributions are illustrated in Figure 1b which we will be calling the low, medium and high-frequency components of the gain variation, bearing in mind of course that their actual frequency range will depend on the carrier frequency **q**. In real-space the side-band becomes:

$$I_q(\boldsymbol{r},\phi) = ae^{i\phi} + ae^{i\phi}g_0(\boldsymbol{r}) + g_q(\boldsymbol{r}) + ae^{-i\phi}g_{2q}(\boldsymbol{r}) \quad (23)$$

The low-frequency term, $g_0(\boldsymbol{r})$, is real with no imaginary part, but the medium, $g_q(\boldsymbol{r})$, and high-frequency, $g_{2q}(\boldsymbol{r})$, terms are in general complex.

The side-band (and centre-band) can in turn be described in terms of the reconstructed amplitude, $A(\boldsymbol{r},\phi)$, and phase, $\Phi(\boldsymbol{r},\phi)$, defined by:

$$I_q(\boldsymbol{r},\phi) \stackrel{\text{def}}{\equiv} A(\boldsymbol{r},\phi)e^{i\Phi(\boldsymbol{r},\phi)} \tag{24}$$

where the capitals emphasise their difference from the input, or original, amplitude and phase. To evaluate the variation from the perfect detector case where the recorded side-band would equal the signal side-band, we introduce the normalised functions such that:

$$\hat{I}_q(\boldsymbol{r},\phi) = I_q(\boldsymbol{r},\phi)/S_q(\boldsymbol{r},\phi) \tag{25}$$

and for the amplitudes and phases, respectively:

$$A(\boldsymbol{r},\phi) = \text{Amp}\big[S_q(\boldsymbol{r},\phi)\big] \times \text{Amp}\big[\hat{I}_q(\boldsymbol{r},\phi)\big] \equiv a\hat{A}(\boldsymbol{r},\phi) \tag{26}$$

and

$$\Phi(\boldsymbol{r},\phi) = \text{Phase}\big[S_q(\boldsymbol{r},\phi)\big] + \text{Phase}\big[\hat{I}_q(\boldsymbol{r},\phi)\big] \equiv \phi + \hat{\Phi}(\boldsymbol{r},\phi) \tag{27}$$

For both the side-bands and the centre-band, the amplitude of the normalised function gives the relative variation, or percentage error, in the amplitude compared to the input signal and the phase of the normalised side-band gives directly the phase error. We will be assuming that the gain variations are small and hence the amplitude of the normalised function be close to one and the imaginary part close to zero. In that case, the corresponding real and imaginary parts will equal the amplitude and phase, respectively, to a very good approximation:

$$\hat{A}(\boldsymbol{r},\phi) \cong Re\big[\hat{I}_q(\boldsymbol{r},\phi)\big] \tag{28}$$

and

$$\hat{\Phi}(\boldsymbol{r},\phi) \cong Im\big[\hat{I}_q(\boldsymbol{r},\phi)\big] \tag{29}$$

Side-band analysis

For the side-band, the result is:

$$\hat{I}_q(\boldsymbol{r},\phi) = 1 + g_0(\boldsymbol{r}) + a^{-1}e^{-i\phi}g_q(\boldsymbol{r}) + e^{-2i\phi}g_{2q}(\boldsymbol{r}) \tag{30}$$

Firstly, the function is clearly complex and will have an effect on both the reconstructed amplitude and phase. Secondly, and perhaps even more crucially, this effect will depend on the phase of the input hologram, ϕ. To understand better, we need to look at the real and imaginary parts:

$$Re\big[\hat{I}_q(\boldsymbol{r},\phi)\big] = 1 + g_0(\boldsymbol{r}) + a^{-1}Re\big[e^{-i\phi}g_q(\boldsymbol{r})\big] + Re\big[e^{-2i\phi}g_{2q}(\boldsymbol{r})\big] \tag{31}$$

$$Im\big[\hat{I}_q(\boldsymbol{r},\phi)\big] = a^{-1}Im\big[e^{-i\phi}g_q(\boldsymbol{r})\big] + Im\big[e^{-2i\phi}g_{2q}(\boldsymbol{r})\big] \tag{32}$$

where we have used the fact that $g_0(\boldsymbol{r})$ is real.

Both the amplitude and the phase depend on the original phase of the hologram, ϕ, except for the low-frequency term present in the amplitude. A subtler feature is that the relative weighting of the terms depends on the input amplitude of the fringes, a. As the visibility improves, the medium-frequency $g_q(\boldsymbol{r})$ term diminishes in influence compared with the low $g_0(\boldsymbol{r})$ and high-frequency $g_{2q}(\boldsymbol{r})$ terms.

The interim conclusion is that the usual procedure of subtracting the phase of a reference hologram to correct the systematic errors will run into problems, as we will show later in detail.

Centre-band analysis

The result for the centre-band, whether normalised or not, is:

$$I_0(\boldsymbol{r},\phi) = \hat{I}_0(\boldsymbol{r},\phi) = 1 + g_0(\boldsymbol{r}) + ae^{i\phi}g_{-q}(\boldsymbol{r}) + ae^{-i\phi}g_q(\boldsymbol{r})$$

$$= 1 + g_0(\boldsymbol{r}) + ae^{i\phi}g_q(\boldsymbol{r})^* + ae^{-i\phi}g_q(\boldsymbol{r})$$

$$= 1 + g_0(\boldsymbol{r}) + 2aRe\left[e^{-i\phi}g_q(\boldsymbol{r})\right] \tag{33}$$

Again, we see that the phase of the hologram will change the contribution from the gain but is not influenced by the high-frequency gain variations.

Pi-shifted holograms

Side-band analysis

The results for the pi-shifted holograms are the following for the side-band:

$$\hat{I}_q^{(-)}(\boldsymbol{r},\phi) = 1 + g_0(\boldsymbol{r}) + e^{-2i\phi}g_{2q}(\boldsymbol{r}) \tag{34}$$

where the normalisation is carried out with respect to the signal, Eq. (25), which is twice as strong as for a single hologram. If we compare with the result from a single hologram, Eq. (30), we can see that the medium-frequency noise term has been eliminated. This term came from the convolution of the signal centre-band with the gain variation, the influence of the centre-band being eliminated from the pi-shifted hologram.

The real and imaginary parts are the following:

$$Re\left[\hat{I}_q^{(-)}(\boldsymbol{r},\phi)\right] = 1 + g_0(\boldsymbol{r}) + Re\left[e^{-2i\phi}g_{2q}(\boldsymbol{r})\right] \tag{35}$$

$$Im\left[\hat{I}_q^{(-)}(\boldsymbol{r},\phi)\right] = Im\left[e^{-2i\phi}g_{2q}(\boldsymbol{r})\right] \tag{36}$$

For completeness, we will include the result for the addition of the pi-shifted side-bands, which in the ideal case would produce zero (see Eq. (14)). However, in the presence of gain variations a non-zero result is obtained:

$$\hat{I}_q^{(+)}(\boldsymbol{r},\phi) = a^{-1}e^{-i\phi}g_q(\boldsymbol{r}) \tag{37}$$

In this case, the result has been normalised with respect to the side-band signal. The medium-frequency noise has not been eliminated by the pi-shifting algorithm but displaced.

Centre-band analysis

The centre-band of the pi-shifted holograms should give a uniform distribution in the absence of noise, Eq. (15), but now will give:

$$\hat{I}_0^{(-)}(\boldsymbol{r},\phi) = 2aRe\left[e^{-i\phi}g_q(\boldsymbol{r})\right] \tag{38}$$

and

$$\hat{I}_0^{(+)}(\boldsymbol{r},\phi) = 1 + g_0(\boldsymbol{r}) \tag{39}$$

The centre-band result has no imaginary part, as must be the case given the masks used (Eq. (8)).

Even for the pi-shifted holograms will be affected by the original phase of the signal but to a lesser degree.

Pixel displacements

After having analysed gain variations, we will now consider the fact that the pixels of a detector never lie on a perfectly regular square array. Their effective positions are slightly displaced from their ideal positions, either because of the fibre optic coupling or the lay-out of the detection electronics [33]. These are known to produce phase variations [1, 6] but the consequences of high-frequency components from abrupt pixel-to-pixel displacements have not been fully appreciated.

We can model these distortions as a vector displacement field, $\mathbf{u}(\mathbf{r})$. Following the same argument as for geometric phase analysis [34], the recorded intensity is related to the input signal in the following way:

$$I(\boldsymbol{r}) = S(\boldsymbol{r} - \boldsymbol{u}(\boldsymbol{r})) \tag{40}$$

For the perfect hologram fringes, this becomes:

$$I(\boldsymbol{r},\phi) = 1 + ae^{i\phi}e^{-2\pi i\boldsymbol{q}.\boldsymbol{u}(\boldsymbol{r})}e^{2\pi i\boldsymbol{q}.\boldsymbol{r}} + ae^{-i\phi}e^{2\pi i\boldsymbol{q}.\boldsymbol{u}(\boldsymbol{r})}e^{-2\pi i\boldsymbol{q}.\boldsymbol{r}} \tag{41}$$

*w*here the familiar geometric phase terms appear. At this point, it is interesting to note that the centre-band is not directly affected by the displacement field, contrary to gain variations. In Fourier space, only the two side-bands will be convoluted with the displacement field distribution. This has consequences for the pi-shifting algorithm later on.

The displacements will be considered small, small compared to the pixel spacing, so to a good approximation:

$$I(\boldsymbol{r},\phi) = S(\boldsymbol{r},\phi) - 2\pi i\boldsymbol{q}.\boldsymbol{u}(\boldsymbol{r})ae^{i\phi}e^{2\pi i\boldsymbol{q}.\boldsymbol{r}} + 2\pi i\boldsymbol{q}.\boldsymbol{u}(\boldsymbol{r})ae^{i\phi}e^{-2\pi i\boldsymbol{q}.\boldsymbol{r}} \tag{42}$$

To simplify the appearance of the equations, we will introduce the scalar function, u, which is the component of the displacement in the direction of the carrier frequency vector, q:

$$u(\boldsymbol{r}) \stackrel{\text{def}}{=} \boldsymbol{q}.\boldsymbol{u}(\boldsymbol{r})/q \tag{43}$$

where q is the modulus of the vector $\mathbf{q}$. In Fourier space, the recorded intensity then becomes:

$$\tilde{I}(\boldsymbol{k},\phi) = \tilde{S}(\boldsymbol{k},\phi) - 2\pi iqae^{i\phi}\tilde{u}(\boldsymbol{k}-\boldsymbol{q}) + 2\pi iqae^{-i\phi}\tilde{u}(\boldsymbol{k}+\boldsymbol{q}) \tag{44}$$

Following the same procedure as for the gain that resulted in Eq. (30), we can arrive at the following relations for the normalised side-bands:

$$\hat{I}_q(\boldsymbol{r},\phi) = 1 - 2\pi i q u_0(\boldsymbol{r}) + 2\pi i q e^{-2i\phi} u_{2q}(\boldsymbol{r}) \tag{45}$$

Given that the low-frequency displacement function is real, the result in terms of the real and imaginary parts, and hence the measured amplitude and phase, is the following:

$$Re\left[\hat{I}_q(\boldsymbol{r},\phi)\right] = 1 - 2\pi q Im\left[e^{-2i\phi} u_{2q}(\boldsymbol{r})\right] \tag{46}$$

$$Im\left[\hat{I}_q(\boldsymbol{r},\phi)\right] = -2\pi q u_0(\boldsymbol{r}) + 2\pi q Re\left[e^{-2i\phi} u_{2q}(\boldsymbol{r})\right] \tag{47}$$

The amplitude of the reconstructed side-band will therefore have systematic noise from the high-frequency displacement field, $u_{2q}(\boldsymbol{r})$, dependent on the initial phase. The phase of the reconstruction will be modified by the low-frequency component of the displacement field, $u_0(\boldsymbol{r})$. It is this component which is usually corrected for using a reference hologram, and accurately so, given that this noise is independent of the initial phase of the hologram.

However, there is also noise from the high-frequency component of the displacement field, $u_{2q}(\boldsymbol{r})$, which will not be eliminated in general by subtracting the phase of a single reference hologram. Contrary to gain variations, Eq. (30), however, the term in frequency $\mathbf{q}$ of the noise, $u_q(\boldsymbol{r})$**,** is absent. This is due to the fact that displacements do not modify the centre-band of the signal directly. However, this term does appear in the centre-band of the reconstruction:

$$\hat{I}_0(\boldsymbol{r},\phi) = I_0(\boldsymbol{r},\phi) = 1 - 2\pi i q a e^{i\phi} u_{-q}(\boldsymbol{r}) + 2\pi i q a e^{i\phi} u_q(\boldsymbol{r}) \tag{48}$$

Using the symmetry between conjugate components, Eq. (11), this simplifies to:

$$\hat{I}_0(\boldsymbol{r},\phi) = I_0(\boldsymbol{r},\phi) = 1 - 4\pi q Im\left[a e^{-i\phi} u_q(\boldsymbol{r})\right] \tag{49}$$

As expected, the centre-band reconstruction is real and has no phase component. However, the amplitude is indeed modulated by noise from the pixel-to-pixel displacements, this time the medium-frequency component, $u_q(\boldsymbol{r})$. This noise depends on the initial phase of the fringes, just like the side-band.

There is no point in considering the pi-shifted holograms for the pixel-to-pixel distortions as we can see that the reconstructed side band, Eq. (45), is unaffected by a change of pi of the signal hologram. No components of the noise will therefore be eliminated using the algorithm and is a direct consequence of the centre-band of the signal not influencing the results, as mentioned previous with respect to Eq. (41).

Results

To test the theory, we have carried out some simulations using scripting in DigitalMicrograph (Gatan Inc.) and hologram processing with HoloDark (HREM Research Inc.), a plugin for DigitalMicrograph. The detector was modelled as having 512 by 512 pixels and illuminated by a perfect hologram with 6-pixel fringe spacing at an angle of 20° to the horizontal. The visibility of

the fringes was 40% giving a fringe amplitude, a, of 0.2 and had different input phases, ϕ, of zero, pi/2 and pi. The detector was considered to have variable gain and pixel-to-pixel distortions but otherwise perfect. The hologram signal was simulated using Eq. (1) and the recorded hologram using Eq. (17) for the gain variations and Eq. (41) for the displacements.

Gain variation simulations

Random numbers with a Gaussian distribution were generated for each pixel and then fixed for all the simulations (see Figure 2a). The standard deviation of the gain variations was 5%. The low, medium and high-frequency gain components appearing in Eq. (23) were extracted from the Fourier transform (see Figure 2b) using Eq. (7) with circular cosine masks, Eq. (10) of radius q/2. The real and imaginary parts of the functions are shown in Fig. 2 b-h. To avoid any possible edge effects, only the central 256 square area is shown for all the Figures.

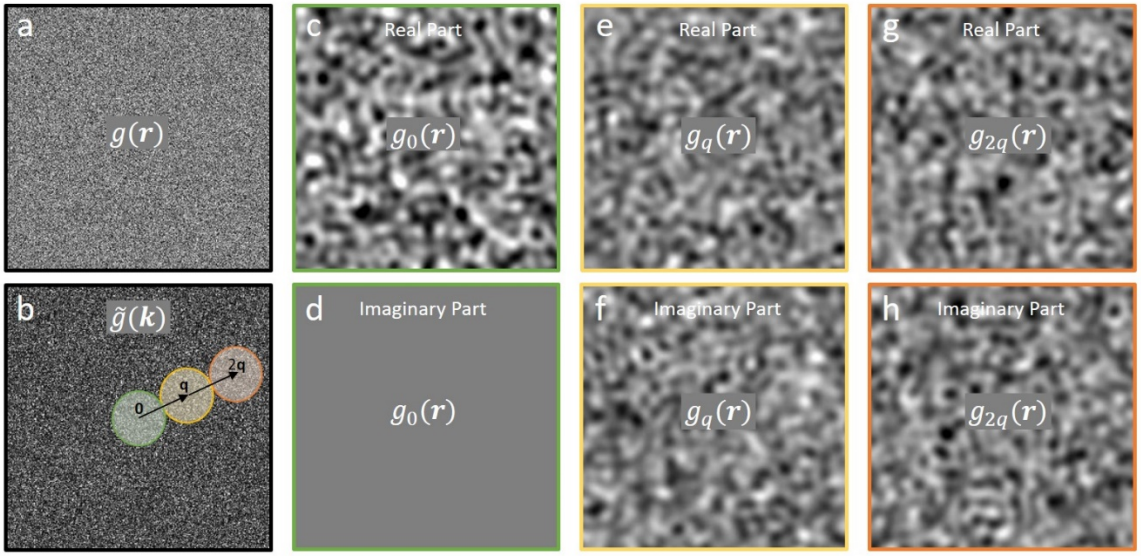

Figure 2. Simulated gain variations: (a) random gain variations; (b) power spectrum of gain variations with masks indicated for low (c,d), medium (e,f) and high frequency components (g,h). Real and Imaginary parts shown for central 256 square area of detector. Grey levels (a) ±15% minimum to maximum (c-h) ±1% minimum to maximum. Standard deviations are: (a) 5% (c) 0.40% (e-h) 0.28%.

As expected, the power spectrum of the gain (Fig. 2b) shows the characteristic white noise speckle, uniformly spread across all frequencies. We can see that the low-frequency term, $g_0(\boldsymbol{r})$, is indeed real with no imaginary part (Fig. 2d) but that the medium, $g_q(\boldsymbol{r})$, and high-frequency, $g_{2q}(\boldsymbol{r})$, terms are complex (Eq. (23)). It is important to point out that there is no correlation between the different components, as they come from different parts of the Fourier transform, and have completely uncorrelated spatial distributions even between real and imaginary parts.

For gain variations of 5% shown here, the standard deviations of the real part of low-frequency term $g_0(\boldsymbol{r})$ is 0.40% whereas the real and imaginary parts of $g_q(\boldsymbol{r})$, and high-frequency, $g_{2q}(\boldsymbol{r})$, have standard deviations of 0.28%. In fact, the standard deviation of the modulus of all the components is 0.40%, the reason for the apparent difference being that the low-frequency term has no imaginary part. The much lower variability in the components compared with the original gain comes from the mask used in the Fourier processing detailed later.

A hologram, simulated and adjusted for the gain directly using Eqs. (1) and (17), is shown in Figure 3a. The side-band was extracted using Eq. (7) with the same cosine mask as previously (Figs. 3c and d). The standard deviation of the amplitude is 1.5% of the average value and the phase 14.1 mrad. To test the theoretical development, the corresponding amplitude and phase (Figs. 3e and 3f) were then calculated instead using Eqs. (31) and (32), respectively, and injecting the gain components calculated in Figure 2. The results of simulations and theory match to within numerical errors.

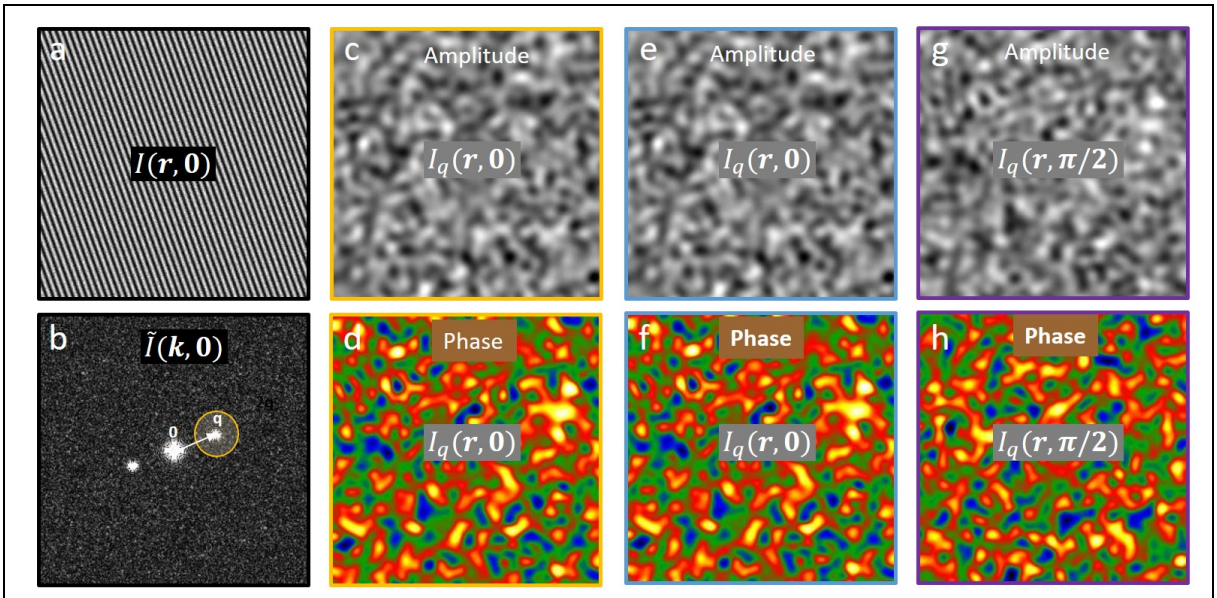

Figure 3. Simulated hologram with 5% gain variations: (a) hologram intensity simulated using Eq. (17); (b) power spectrum with mask indicating side-band extraction; (c) reconstructed relative amplitude; (d) corresponding reconstructed phase (in colour); (e) theoretical relative amplitude using Eq. (31); (f) theoretical phase using Eq. (32); (g) reconstructed relative amplitude for simulation with initial phase of π/2; (h) corresponding relative phase. Grey levels (c,e,g) ±1% minimum to maxium; Colour range (d,f,h) ±50 mrad black to white. Standard deviations are: (c,e,g) 1.5% of the amplitude; (d,f,h)14.1 mrad in the phase.

Also shown on Figure 3 are the amplitude and phase for a simulated hologram with initial phase of $\pi/2$. The amplitude and phase systematic noise (Figs. 3g and 3h respectively) are very different

to that from the hologram with an initial phase of zero (Fig. 3c and 3d). Subtracting the two hologram phases would therefore increase, not eliminate, the noise from gain variations.

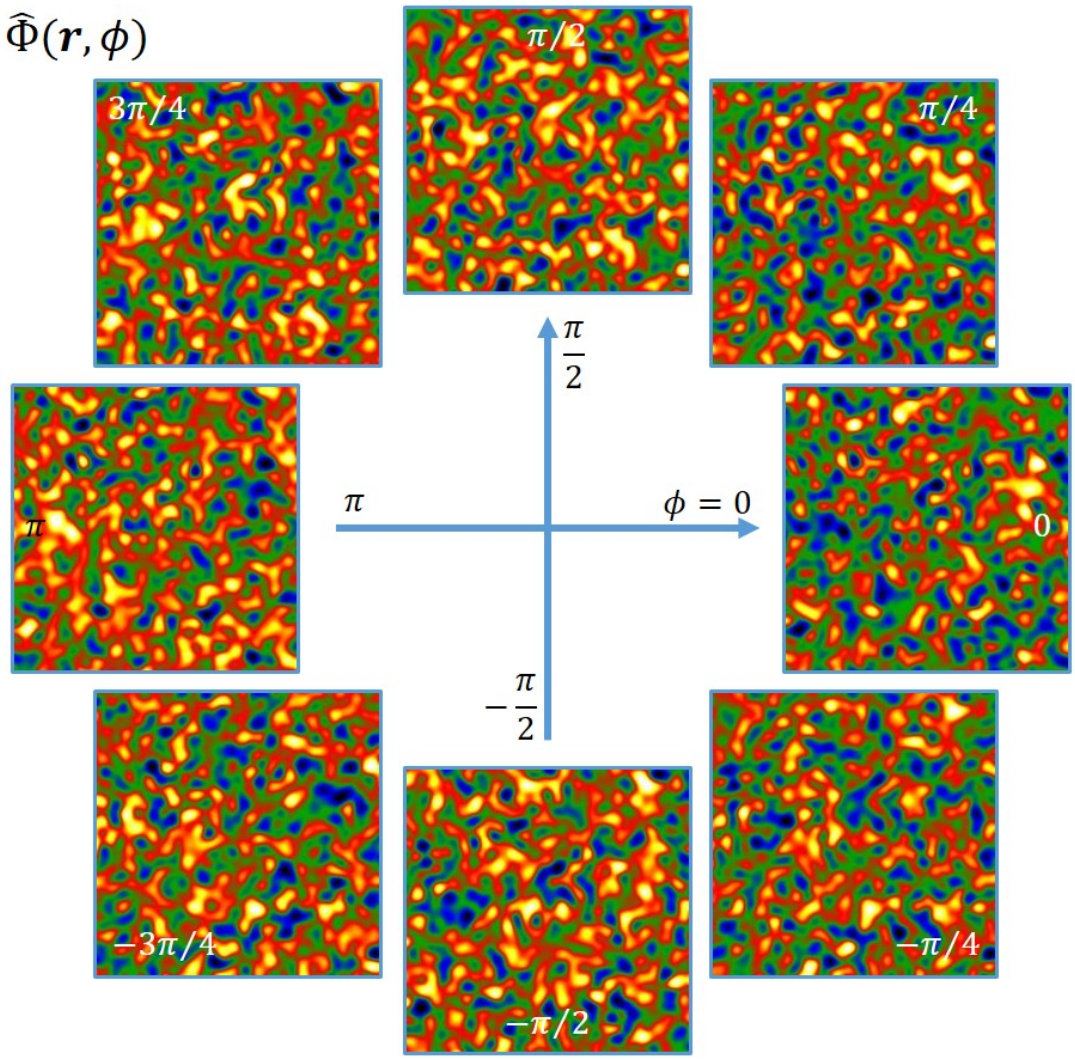

Figure 4. Phase noise from 5% gain variation as a function of initial phase, ϕ: theoretical relative phase $\widehat{\Phi}(\boldsymbol{r},\phi)$ calculated using Eq. (32). Colour range: ±50 mrad black to white.

We can easily calculate the relative phase for any other value of initial phase, ϕ, using Eq. (32). These are shown on Figure 4 for initial phases from 0 to 2π in steps of $\pi/4$. The phase noise changes gradually over the cycle. Because the two terms in Eq. (32) cycle differently, every phase image is different. The dominant term depends on the medium-frequency component $g_q(\boldsymbol{r})$ which inverts on changing the initial phase by π. However, the other term depending on the high-frequency term $g_{2q}(\boldsymbol{r})$ does not.

The analysis of a simulated pi-shifted hologram, calculated from two simulated holograms using Eq. (6), is shown in Figure 5. The centre-band is indeed absent from the Fourier transform (Fig. 5b). The amplitude and phase variations are much smaller (Figs. 5c and 5d) than in Figure 3, given the absence of terms in the theoretical expressions Eqs. (35) and (36) respectively (Figs. 5e and 5f). Indeed, the standard deviations for the relative amplitude and phase are now only 0.51% and 2.9 mrad, respectively.

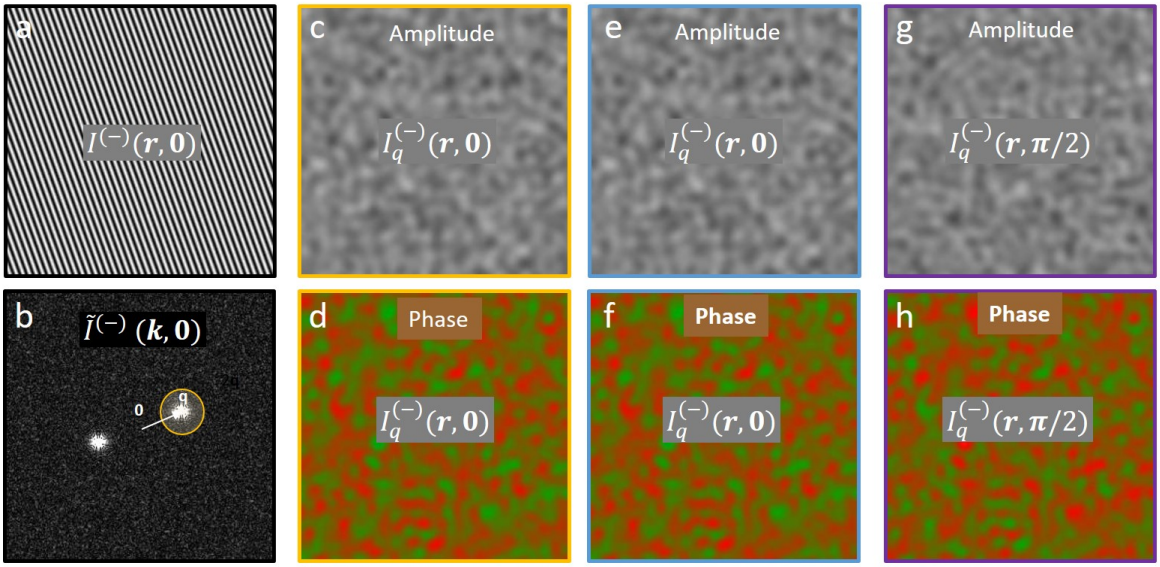

Figure 5. Simulated pi-shifted hologram with 5% gain variation: (a) pi-shifted hologram intensity; (b) power spectrum with mask indicating side-band extraction; (c) reconstructed relative amplitude; (d) corresponding reconstructed phase (in colour); (e) theoretical relative amplitude using Eq. (35); (f) theoretical phase using Eq. (36); (g) reconstructed relative amplitude for initial phase of π/2; (h) corresponding relative phase. Grey levels (c,e,g) ±1% minimum to maxium; Colour range (d,f,h) ±50 mrad black to white. Standard deviations are: (c,e,g) 0.51% of the amplitude; (d,f,h) 2.9 mrad in the phase.

Figures 5g and 5h show the amplitude and phase determined from a pi-shifted hologram with calculated from the holograms of initial phases of π/2 and 3π/2. The phase (Fig. 5h) is exactly inverted with respect to pi-shifted hologram at zero initial phase (Fig. 5d), as expected from Eq. (36). In this case, subtracting the two reconstructed phases would exactly double the noise.

Pixel displacement simulations

We can carry out a similar analysis for the pixel-to-pixel displacements. This time, a random displacement field was simulated having a standard deviation of 0.05 pixels in both x and y directions. The corresponding holograms were calculated using Eq. (41) and the same fringe visibility and carrier frequency as before. A hologram having and initial phase of zero is shown in Figure 6a.

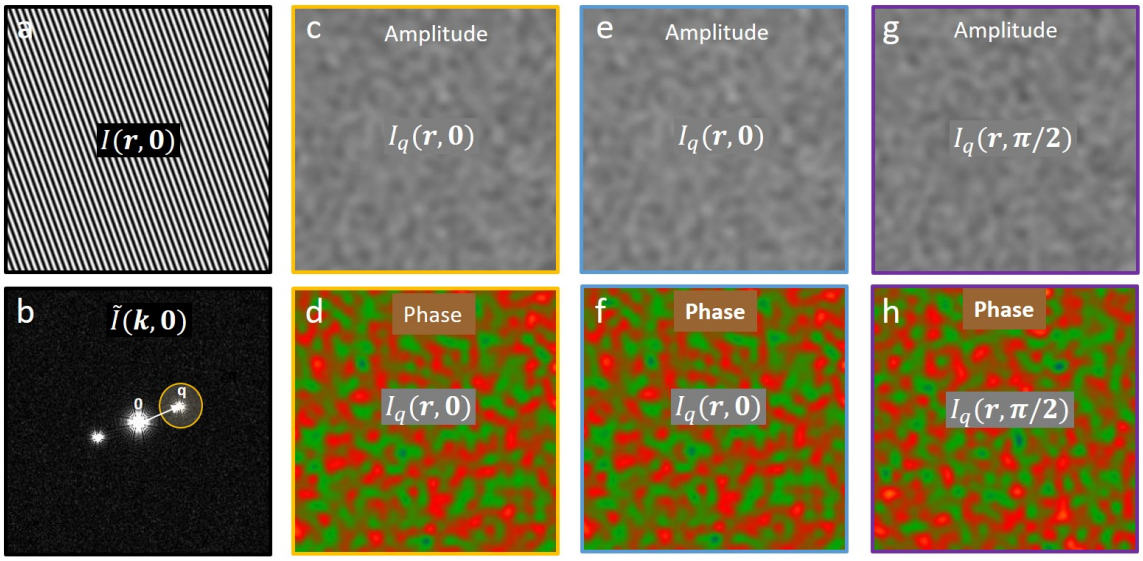

Figure 6. Simulated hologram with pixel-to-pixel displacements: (a) hologram simulated using Eq. (41); (b) power spectrum with mask indicating side-band extraction; (c) reconstructed relative amplitude; (d) corresponding reconstructed phase (in colour); (e) theoretical relative amplitude using Eq. (46); (f) theoretical phase using Eq. (47); (g) reconstructed relative amplitude for initial phase of π/2; (h) corresponding relative phase. Grey levels (c,e,g) ±1% minimum to maxium; Colour range (d,f,h) ±50 mrad black to white. Standard deviations are: (c,e,g) 0.29% of the amplitude; (d,f,h) 5.1 mrad in the phase.

Again, the simulation (Figs. 6c and 6d) using Eq. (41) and theory (Figs. 6e and 6f) using Eqs. (46) and (47), agree to within numerical errors. The standard deviations for the relative amplitude and phase are 0.29% and 5.1 mrad respectively. For an initial phase of π/2, the spatial distribution of the noise is different (Figs. 6g and 6h). In fact, the amplitude noise is exactly inverted, whereas the phase appears uncorrelated. This is because only the high-frequency distortion terms inverts (Eq. (46)) whilst the low-frequency distortion term stays the same.

Discussion

Gain variations and pixel displacements produce phase variations which look like random noise (see Figs. 3-6). However, the variations can be determined directly from the static gain and displacement distributions, through Eqs. (32) and (47) respectively. Unfortunately, these distributions are difficult to determine experimentally with sufficient accuracy. Gain varies from day to day and geometric distortions, though stable, are difficult to measure accurately at the scale of individual pixels. The only solution is to consider them as a fatality, similar to random noise, or try to correct them. We will begin by estimating the resulting standard deviation in the phase.

The variations of the relevant gain and displacement components will be lower than the initial standard deviation (cf Fig. 2) depending on the mask used. The reduction factor has been

calculated for hard binary masks [35]. An extension to other masks, like the cosine mask used here, shows that the variance is multiplied by a factor equal to the integral of the square of the mask in Fourier space. Some tedious integration of the cosine mask, Eq. (10), gives the following result for the standard deviation factor, f_M:

$$f_M = k_M\sqrt{\frac{\pi}{2}-\frac{2}{\pi}} = 0.967k_M \tag{50}$$

The mask radius, k_M, expressed in pixels^{-1}, is less than 0.5 (Nyquist) and therefore the factor is always less than one for any mask. In our case, the mask radius is q/2 giving:

$$f_M = \frac{q}{2}\sqrt{\frac{\pi}{2}-\frac{2}{\pi}} = 0.484q \tag{51}$$

By comparison, a hard square mask of side q would give [35]:

$$f_M = q \tag{52}$$

The standard deviation of the real and imaginary parts of the medium and high-frequency components are $\sqrt{2}$ smaller when taken individually. For a given standard deviation of the gain variations, σ_g, they follow the relation:

$$\sigma\big(g_0(\boldsymbol{r})\big) = \sqrt{2}\sigma\big(Re\big[g_q(\boldsymbol{r})\big]\big) = \sqrt{2}\sigma\big(Im\big[g_q(\boldsymbol{r})\big]\big) = f_M\sigma_g \tag{53}$$

For our fringe spacing of 6 pixels, the mask factor is 0.081 using Eq. (51), giving for a gain variation of 5% a standard deviation of 0.40% for the low-frequency component and 0.28% for the real and imaginary parts of the others. These values reproduce exactly the standard deviations measured from the simulations (Fig. 3).

We have already seen that the noise appears lower in the pi-shifted holograms in the presence of gain variations (cf Figs. 3 and 5). Assuming that the different components are indeed uncorrelated, the standard deviation of the phase due to non-uniform gain can be estimated from Eq. (32) by summing the variances:

$$\sigma_g\big(\widehat{\Phi}\big) = \frac{1}{2}f_M\sigma_g\sqrt{a^{-2}+1} \tag{54}$$

The corresponding result for the pi-shifted holograms, Eq. (47), is:

$$\sigma_g\big(\widehat{\Phi}^{(-)}\big) = \frac{1}{2}f_M\sigma_g \tag{55}$$

We would therefore expect the pi-shifted hologram to have noise lowered by a factor of $\sqrt{a^{-2}+1}$, or in our case about 5. The actual values from the simulations are 14.1 mrad (Fig. 3) and 2.9 mrad (Fig. 4) respectively, giving a reduction of 4.9. Indeed, any improvement seen in experiments on pi-shifting could be indicative of poor gain normalisation.

For the distortion, similar analysis applied to Eq. (47) results in:

$$\sigma_u(\widehat{\Phi}) = 2\pi q\sqrt{\frac{3}{2}} f_M \sigma_u \tag{56}$$

The standard deviation calculated for the simulation is 5.1 mrad, which agrees with the measured value (Figure 6). A systematic increase in the phase noise with carrier frequency (but keeping the same mask size, see Eqs. (50) and (51)) might be indicative of high-frequency pixel displacements. Unfortunately, other sources of noise typically increase with carrier frequency. No improvement should be visible in the pi-shifted holograms.

The question is whether these values can be improved by correction using the standard procedure of subtracting the phase of a reference hologram, given that we have shown that the variations depend on the original phase of the signal (cf Fig. 4). If all the conditions are identical, including the initial phase of the hologram, the systematic terms will all be eliminated. However, there is no certainty that the reference hologram would be acquired with the same phase, barring automation [16]. Indeed, the hologram of a real object will have a varying phase over the field of view. Locally, the object hologram and reference hologram will not have the same phase in general.

Imagine correcting the phase using a reference hologram of phase, ϕ^{ref}:

$$\widehat{\Phi}^{\mathrm{corr}}(\boldsymbol{r}, \phi, \phi^{\mathrm{ref}}) = \widehat{\Phi}^{\mathrm{raw}}(\boldsymbol{r}, \phi) - \widehat{\Phi}^{\mathrm{ref}}(\boldsymbol{r}, \phi^{\mathrm{ref}}) \tag{57}$$

From Eq. (29), it follows that:

$$\widehat{\Phi}^{\mathrm{corr}}(\boldsymbol{r}, \phi, \phi^{\mathrm{ref}}) \simeq Im\left[\hat{I}_q(\boldsymbol{r}, \phi)\right] - Im\left[\hat{I}_q(\boldsymbol{r}, \phi^{\mathrm{ref}})\right] \tag{58}$$

For gain variations, Eq. (32), this means:

$$\widehat{\Phi}^{\mathrm{corr}}(\boldsymbol{r}, \phi, \phi^{\mathrm{ref}}) = Im\left[\left(e^{-i\phi} - e^{-i\phi^{\mathrm{ref}}}\right) g_q(\boldsymbol{r})\right] + Im\left[\left(e^{-2i\phi} - e^{-2i\phi^{\mathrm{ref}}}\right) g_{2q}(\boldsymbol{r})\right] \tag{59}$$

Now expressing the phase difference as:

$$\Delta\phi \stackrel{\mathrm{def}}{=} \phi^{\mathrm{ref}} - \phi \tag{60}$$

we come to the following result:

$$\widehat{\Phi}^{\mathrm{corr}}(\boldsymbol{r}, \phi, \phi^{\mathrm{ref}}) = 2\mathrm{a}^{-1} \sin(\Delta\phi/2)\, Im\left[ie^{-i\Delta\phi/2} e^{-i\phi} g_q(\boldsymbol{r})\right] + 2\sin(\Delta\phi)\, Im\left[ie^{-i\Delta\phi} e^{-2i\phi} g_{2q}(\boldsymbol{r})\right] \tag{61}$$

There are two terms with different behaviour. If the phase of the reference hologram is the same as the target hologram, the corrected phase is zero. This is the signature of systematic errors: repeating an identical experiment will produce exactly the same result. However, the reference hologram is more likely to have a different phase as explained previously. If the phase difference is π, for example, then:

$$\widehat{\Phi}^{\mathrm{corr}}(\boldsymbol{r}, \phi, \phi^{\mathrm{ref}}, \Delta\phi = \pi) = 2\mathrm{a}^{-1} Im\left[e^{-i\phi} g_q(\boldsymbol{r})\right] \tag{62}$$

and the noise is far from being eliminated on correction.

The pi-shifted holograms, however, have only one term, giving the following result:

$$\widehat{\Phi}^{\mathrm{corr}}(\boldsymbol{r},\phi,\phi^{\mathrm{ref}}) = 2\sin(\Delta\phi)\,Im\left[ie^{-i\Delta\phi}e^{-2i\phi}g_{2q}(\boldsymbol{r})\right] \tag{63}$$

This shows that the maximum error is obtained when the two holograms are $\pi/2$ out of phase, doubling the initial noise level from the gain (cf Figs. 5d and 5h). Using the previous expressions for the standard deviations, Eq. (53):

$$\sigma_g\left(\widehat{\Phi}^{\mathrm{corr}}\right) = f_M\sigma_g\sqrt{\mathrm{a}^{-2}\sin^2(\Delta\phi/2)+\sin^2(\Delta\phi)} \tag{64}$$

and for the pi-shifted hologram:

$$\sigma_g\left(\widehat{\Phi}^{(\text{-})\mathrm{corr}}\right) = f_M\sigma_g|\sin(\Delta\phi)| \tag{65}$$

For the distortions, Eq. (47), the result is similar to the pi-shifted gain variations:

$$\widehat{\Phi}^{\mathrm{corr}}(\boldsymbol{r},\phi,\phi_{\mathrm{ref}}) = 4\pi\mathrm{q}\sin(\Delta\phi)\,Im\left[ie^{-i\Delta\phi}e^{-2i\phi}u_{2q}(\boldsymbol{r})\right] \tag{66}$$

The low-frequency term has been completely eliminated, leaving only the high-frequency term. The corresponding standard deviation of the corrected phase will be:

$$\sigma_u\left(\widehat{\Phi}^{\mathrm{corr}}\right) = 2\pi q\sqrt{2}f_M\sigma_u|\sin(\Delta\phi)| \tag{67}$$

Using the values for our simulations, we can present Eqs. (64), (65) and (67) as a function of the phase shift between object and reference hologram to demonstrate the salient features (Figure 7). We can see that for the gain variations (Fig. 7a) the residual phases are in general much smaller for the pi-shifted holograms than for the individual holograms, corrected or otherwise, and that only very particular values of the relative phases completely eliminate the noise. For intermediate values, the noise in the corrected phase can even be bigger than for the raw holograms. The results for the pixel displacements (Fig. 7b) follow a similar trend. However, correction usually improves the phase noise because the low-frequency component is eliminated.

Of course, the actual amount of detector noise, as illustrated in Fig. 7, will depend on the mask size and the standard deviations of the gain and pixel displacements. We chose the values of 5% gain variation and 5% of the pixel spacing as being representative. These values could be the residuals after (imperfect) calibration and correction of gain and geometric distortion. Indeed, gain normalisation is not necessarily easy to perform to high accuracy for every experiment. Even DDD cameras operating in so-called counting mode, where electrons are detected individually, have a gain variation representing the fact that some pixels have a higher probability of detecting an electron than others. On the other hand, pixel displacements are likely to be smaller in DDD cameras than CCD cameras, due to the lack of fibre-optic coupling, but without experimental verification it is hard to say.

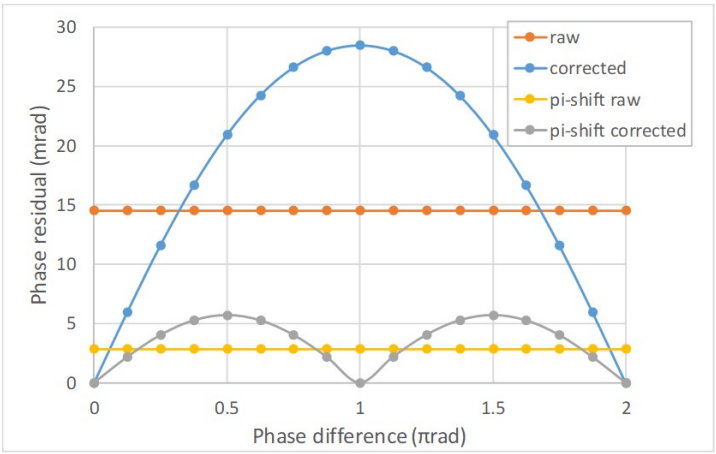

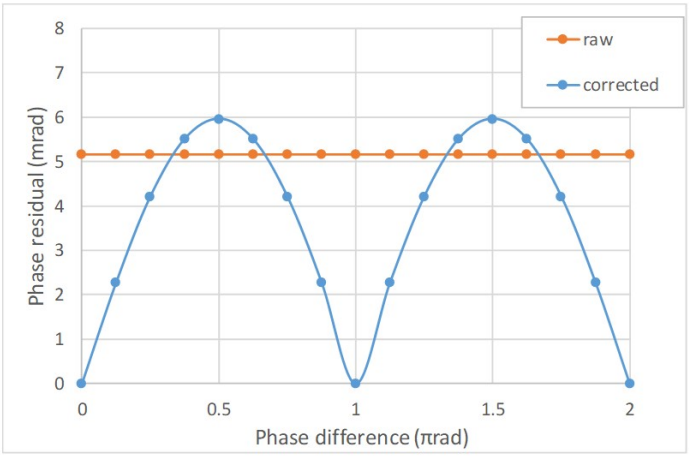

Figure 7. Phase errors before (raw) and after reference hologram correction (corrected), as a function of the phase-shift between object and reference holograms: (a) gain; (b) distortion. Gain variations were 5%, pixel displacements 0.05, hologram fringe spacing 6 pixels, visibility 40% and cosine mask radius q/2.

Conclusions

Residual gain variations and non-uniformity in the spatial distribution of pixels will introduce amplitude and phase variations which look like random noise. They are, however, completely deterministic given complete knowledge of the detector characteristics. Analytical expressions have been given (see for example, Eqs. (32) and (47)) and estimates of the standard deviations proposed (see Eqs. (54) and (56)). Gain variations will have a much lesser effect on pi-shifted holograms, confirming if need be the interest of this technique.

With perfect knowledge of the detector in terms of gain variation and pixel distortions, these errors could be calculated and possibly removed from the reconstructed phase. The case of a varying object phase has not been analysed neither has the combination of gain and pixel distortions. It also remains to be seen if experimental methods can be developed to measure these characteristics independently with sufficient ease and accuracy. The standard procedure of using a reference hologram cannot eliminate the noise given that the phase variations depend on the

precise position of the hologram fringes with respect to the detector. Only when the phase of the object and reference holograms are identical over the whole field of view will the noise be eliminated, a rather limited case.

Nevertheless, it should not be concluded that reference holograms are not useful. In fact, they are essential to correct all the other sources of systematic error in the phase. For example, projector lens distortions and biprism charging produce phase variations orders of magnitude larger than those presented here. We are saying, however, that they will not eliminate all sources of error. Indeed, it is likely that the only sources of error remaining in holography experiments, in the vacuum at least, will be the errors from the detector whether they be CCD or DDD. In the light of these results, new procedures for camera calibration may require investigation.

Acknowledgements

The research leading to these results has received funding from the European Union Horizon 2020 research and innovation programme under grant agreement No. 823717 – ESTEEM3. This work has been supported by the French National Research Agency under the "Investissement d'Avenir" program reference No. ANR-10-EQPX-38-01.

References

[1] De Ruijter W J and Weiss J K (1993) Detection limits in quantitative off-axis electron holography. *Ultramicroscopy* 50: 269-283.

[2] Ru Q, Lai G, Aoyama K, Endo J, and Tonomura A (1994) Principle and application of phase-shifting electron holography. *Ultramicroscopy* 55: 209-220.

[3] Harscher A and Lichte H (1996) Experimental study of amplitude and phase detection limits in electron holography. *Ultramicroscopy* 64: 57-66.

[4] Cooper D, Truche R, Rivallin P, Hartmann J-M, Laugier F, Bertin F, Chabli A, and Rouvière J-L (2007) Medium resolution off-axis electron holography with millivolt sensitivity. *Appl. Phys. Lett.* 91 : 143501.

[5] Lichte H (2008) Performance limits of electron holography. *Ultramicroscopy* 108 : 256-262.

[6] Voelkl E and Tang D (2010) Approaching routine 2π/1000 phase resolution for off-axis type holography. *Ultramicroscopy* 110: 447–459

[7] McLeod RA, Bergen M, and Malac M (2014) Phase measurement error in summation of electron holography series. *Ultramicroscopy* 141: 38–50.

[8] Rau W D, Schwander P, Baumann F H, Höppner W, and Ourmazd A (1999) Two-dimensional mapping of the electrostatic potential in transistors by electron holography. *Phys. Rev. Lett.* 82: 2614-2617.

[9] Twitchett A C, Dunin-Borkowski R E, and Midgley P A (2002) Quantitative electron holography of biased semiconductor devices. *Phys. Rev. Lett.* 88: 238302.

[10] McCartney M R, Dunin-Borkowski R E, and Smith D J (2019) Quantitative measurement of nanoscale electrostatic potentials and charges using off-axis electron holography: developments and opportunities. *Ultramicroscopy* 203: 105-118.

[11] Dunin-Borkowski R E, McCartney M R, Smith D J, and Parkin S S P (1998) Towards quantitative electron holography of magnetic thin films using in situ magnetization reversal. *Ultramicroscopy* 74: 61-73.

[12] Gatel C, Bonilla F J, Meffre A, Snoeck E, Warot-Fonrose B, Chaudret B, Lacroix L-M, and Blon T (2015) Size-specific spin configurations in single iron nanomanet: from flower to exotic vortices. *Nano Letters* 15: 6952−6957.

[13] Hÿtch M J, Houdellier F, Hüe F, and Snoeck E (2008) Nanoscale holographic interferometry for strain measurements in electronic devices. *Nature* 453: 1086-1089.

[14] Hÿtch M J, Houdellier F, Hüe F, and Snoeck E (2011) Dark-field electron holography for the measurement of geometric phase. *Ultramicroscopy* 111: 1328–1337.

[15] Lichte H, Herrmann K-H, and Lenz F (1987) Electron noise in off-axis image plane holography. *Optik* 77: 135-140.

[16] Gatel C, Dupuy J, Houdellier F, and Hÿtch M J (2018) Unlimited acquisition time in electron holography by automated feedback control of transmission electron microscope. *Appl. Phys. Lett.* 113: 133102.

[17] Gajdardziska-Josifovska M, McCartney M R, De Ruijter W J, Smith D J, Weiss J K, and Zuo J M (1993) Accurate measurements of mean inner potential of crystal wedges using digital electron holograms. *Ultramicroscopy* 50: 285-299.

[18] McCartney M R (2005) Characterization of charging in semiconductor device materials by electron microscopy. *J. Electron Microscopy* 54: 239-242.

[19] Park J B, Niermann T, Berger D, Knauer A, Koslow I, Weyers M, Kneissl M, and Lehmann M (2014) Impact of electron irradiation on electron holographic potentiometry. *Appl. Phys. Lett.* 105: 094102.

[20] Suzuki H, Akase A, Niitsu K, Tanigaki T, and Shindo D (2017) Secondary electron effect on electron beam induced charging of SiO_2 particle analysed by electron holography. *Microscopy* 66: 167-171.

[21] Cooper D, Ailliot C, Barnes J-P, Hartmann J-M, Salles P, Benassayag G, and Dunin-Borkowski R E (2010) Dopant profiling of focused ion beam milled semiconductors using off-axis electron holography: reducing artifacts, extending detection limits and reducing the effects of gallium implantation. *Ultramicroscopy* 110: 383–389.

[22] Gribelyuk M A, Mody J, Kaganer E, Furkay S S, Miller J, and Charsky A (2019) Sample preparation by focused ion beam without argon ion milling for quantitative electron holography of p-n junctions. *J. Appl. Phys.* 126: 065702.

[23] Lehmann M (2004) Influence of the elliptical illumination on acquisition and correction of coherent aberrations in high-resolution electron holography. *Ultramicroscopy* 100: 9-23.

[24] Lichte H, Geiger D, Harscher A, Heindl E, Lehmann M, Malamidis D, Orchowski A, and Rau W D (1996) Artefacts in electron holography. *Ultramicroscopy* 64: 67-77.

[25] Hüe F, Johnson C L, Lartigue-Korinek S, Wang G, Buseck P R, and Hÿtch M J (2005) Calibration of projector lens distortions. *J. Electron Microscopy* 54: 181-190.

[26] Harada K, Tonomura A, Togawa Y, Akashi T, and Matsuda T (2004) Double-biprism electron interferometry. *Appl. Phys. Lett.* 84: 3229-3231.

[27] Niermann T and Lehmann M (2014) Averaging scheme for atomic resolution off-axis electron holograms. *Micron* 63: 28-34.

[28] Volkov V V, Han M G, and Zhu Y, (2013) Double resolution electron holography with simple Fourier transform of fringe-shifted holograms. *Ultramicroscopy* 134: 175–184.

[29] Boureau V, McLeod R, Mayall B, and Cooper D (2018) Off-axis electron holography combining summation of hologram series with double-exposure phase-shifting: theory and application. *Ultramicroscopy* 193: 52-63.

[30] Krivanek O L and Mooney P E, (1993) Applications of slow-scan CCD cameras in transmission electron microscopy. *Ultramicroscopy* 49: 95-108.

[31] De Ruijter W J (1995) Imaging properties and applications of slow-scan charge-coupled device cameras suitable for electron microscopy. *Micron* 26: 247-275.

[32] Hÿtch M J (1997) Analysis of variations in structure from high resolution electron microscope images by combining real space and Fourier space information. *Microsc. Microanal. Microstruct.* 8: 41–57.

[33] Coleman C I (1985) Imaging characteristics of rigid coherent fiber optic tapers. *Advances in Imaging and Electron Physics* 64: 649-661.

[34] Hÿtch M J, Snoeck E, and Kilaas R (1998) Quantitative measurement of displacement and strain fields from HREM micrographs. *Ultramicroscopy* 74: 131–146.

[35] Chang S L Y, Dwyer C, Barthel J, Boothroyd C B, and Dunin-Borkowski R E (2016) Performance of a direct detection camera for off-axis electron holography. *Ultramicroscopy* 161: 90-97.